Chapter 5
Metal Single-Insulator and Multi-Insulator Diodes for Rectenna Solar Cells

Sachit Grover and Garret Moddel

Abstract Metal/insulator/metal (MIM) diodes work on the inherently fast mechanism of tunneling and have been used in a number of high-frequency applications. This makes them a promising candidate as the rectifying element in rectenna solar cells. In this chapter we describe the operating mechanism of these diodes and review the work done on using them in rectennas. We also provide a simulation methodology to accurately model low-barrier MIM diodes that are used in rectennas. Analytical models based on the WKB method for probability of tunneling are not well suited for analyzing such diodes. We simulate single-insulator (MIM) diodes with varying asymmetry to point out their limited nonlinearity. We also simulate double-insulator (MIIM) diodes that have improved nonlinearity as compared to MIM diodes providing a path for designing more efficient multi-insulator diodes.

5.1 Introduction

An MIM tunnel diode is made of two metal electrodes spaced apart by an extremely thin (few nanometers) insulator. In the MIM diode, the metals have a higher work function than the electron affinity of the insulator producing a barrier at the metal/insulator interfaces as shown in the energy-band profile in Fig. 5.1.

Charge transport across the insulator occurs due to quantum-mechanical tunneling [1] of electrons. A transmission probability is associated with the likelihood of an electron tunneling through the classically forbidden region of an

S. Grover (✉)
National Center for Photovoltaics, National Renewable Energy Laboratory,
15013 Denver West Parkway, Golden, CO 80309-0425, USA
e-mail: sachit.grover@ieee.org

G. Moddel
Electrical Computer & Energy Engineering, University of Colorado,
425 CUB, Boulder, CO 80309-0425, USA
e-mail: moddel@colorado.edu

G. Moddel and S. Grover (eds.), *Rectenna Solar Cells*,
DOI 10.1007/978-1-4614-3716-1_5,

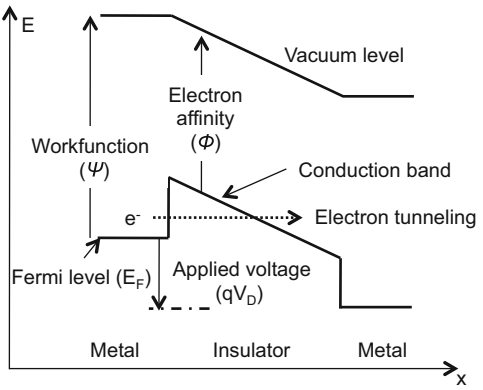

Fig. 5.1 Energy-band profile of an MIM diode, showing the band edge energies as a function of position

insulator bandgap. This probability has a nonlinear dependence on the thickness and height of the barrier [2], whose shape changes with the voltage across the diode. This gives rise to the nonlinear dependence of the tunnel current on the applied voltage and hence the diode characteristics. Most often, these characteristics are modeled using the WKB approximation. However, as we show in this chapter, the WKB method overestimates the tunnel current in low-barrier diodes that are needed in rectennas.

Electron tunneling in MIM junctions occurs on a femtosecond timescale [3]. This inherently fast charge transport across the tunnel barrier allows MIM diodes to operate at optical frequencies. To ensure that tunneling, as opposed to bulk-limited conduction, is the dominant conduction mechanism, the thickness of the insulating layer should not be more than a few nanometers [4].

Historically, point-contact MIM diodes were made by pressing a thin metal wire against an oxidized sheet of metal [5]. These cat's whisker diodes achieve small junction areas without requiring fine lithography. Point-contact diodes use a simple fabrication technique that can test several metal wires for the same oxidized metal sheet at a high throughput [6]. This technique for rapid prototyping is the subject of Chap. 15. Point-contact MIM diodes have been successfully used in experiments on the detection and mixing of infrared radiation [7] and in the frequency characterization of laser lines in the infrared [8].

Significant progress in lithography has allowed small area MIM diodes to be made more reliably. The insulator can be a grown oxide obtained by oxidizing a metal film to the desired thickness, followed by the deposition of a second metal. Alternatively, depositing a stack of metals and insulators provides the freedom to choose the barrier materials independent of the metals. These methods allow the MIM tunnel barrier to be formed without breaking vacuum, preventing contamination at the metal/insulator interfaces. Controlling the roughness of the deposited films is also an important consideration and is discussed in Chap. 6.

A major impediment for the use of MIM diodes in optical rectennas is the large RC time constant of the rectenna circuit using MIM diode [9, 10]. The requirement for a low RC time constant requiring a small diode resistance and capacitance is discussed in Chap. 2.

In this chapter, we investigate the properties of MIM diodes for use in optical rectennas. In Sect. 5.2 we give a brief overview of previous work on infrared rectennas that use MIM diodes. In Sect. 5.3 we describe the parameters and characteristics of MIM diodes relevant for rectification. In Sect. 5.4 we develop a simulation methodology for finding the tunnel current vs. voltage [$I(V)$] characteristics of these diodes. In Sect. 5.5 we carry out a simulation-based analysis of the properties of single-insulator MIM diodes. In Sect. 5.6 we investigate the properties of double-insulator MIIM diodes and compare their performance to MIM diodes. Sections 5.4, 5.5, 5.6 are based on our publication simulating and comparing the characteristics of single- and double-insulator tunnel diodes [11].

5.2 History of MIM Diodes in Rectennas

MIM diodes have shown promise in a variety of high-frequency applications such as frequency measurement in the infrared [12], as infrared detectors [13], and in the emerging field of terahertz electronics [14]. MIM diodes are also used for detection and mixing of radiation in millimeter wave and submillimeter wave bands [15–17]. A fast response time makes these diodes the most likely contender for use in the 60–100 THz, or even a higher, frequency spectrum.

A comparison of detector performance extracted from several references is provided in the table below. The performance is listed as current or voltage responsivity. As discussed in Sect. 5.3.2, responsivity is a measure of how well a diode rectifies. Alternatively, noise equivalent power (NEP) is used as a performance measure, which accounts for the noise along with the responsivity.

References	Performance	Wavelength (μm)
Wang et al. [18]	80 nA/W	10.6
Codreanu et al. [19]	–	10.6
Yamagisha et al. [20]	0.06 V/W	10.6
Adbel-Rahman et al. [16]	NEP = 180 pW/√Hz	10.6
Fumeaux et al. [15]	3.5 mV/W	10.6
Kazemi et al. [21]	10^{-4} V/Wcm^2	3–5
Marchetti et al. [22]	10 μV/W	10.6
Tiwari et al. [23]	NEP = 1.53 nW/√Hz	10.6
Estes et al. [24]	2 mA/W	10.6
Hobbs et al. [25]	0.08 A/W	1.6

Small signal circuit analysis of the lumped-element detector [9] reveals two features that determine its performance. Impedance match between the antenna and the diode and high power-conversion efficiency in the tunnel diode is necessary to achieve efficient rectification. Using analytical models, it has been suggested [9] that a diode with an area of 10×10 nm^2 and an MIM barrier with a thickness of 2 Å is required for optimal performance at 100 THz. This presents the twofold problem of the practicality of such a device and the accuracy of analytical

techniques in modeling high-current, low-barrier diodes. Using accurate simulations, we investigate characteristics of realistic structures. As we find in Sect. 5.5, low resistance typically leads to low responsivity.

To facilitate the match of the diode to the antenna, most researchers have used a low-resistance Ni–NiO–Ni [15, 25] barrier, which has a small nonlinearity. Moreover, at infrared frequencies, using Ni leads to greater resistive losses in the metal as compared to using Au, Ta, or Nb. High-frequency resistance losses depend on the complex dielectric constant. In Sect. 5.6, we show simulation results that compare the resistance and responsivity of several diodes including Ni single-insulator and Ta+Nb multi-insulator diodes. For double-insulator diodes, the responsivity is much larger while maintaining low resistance at zero bias. This better responsivity of multi-insulator diodes [26] has been an important element of the research done in our group.

To overcome the problem of impedance matching, a waveguide-integrated tunnel-junction detector (referred to as traveling-wave detector) [13, 14] was proposed by our group and tested for various wavelengths including 10.6 and 1.5 μm. A version of this device operating at 1.5 μm was fabricated by an IBM group [25]. The IBM implementation is not exactly an antenna-coupled waveguide. Their antenna-coupled waveguide junction is placed on top of a Si-SiO_2 waveguide from which energy may couple via the antenna and also by a direct coupling between the optical and the MIM waveguides.

5.3 Parameters for Characterizing MIM Diodes

Various parameters are used to characterize MIM diodes for use in rectenna solar cells. These parameters are directly related to the diode's band structure. In Fig. 5.2, we label the key aspects of the band diagram for an MIM diode.

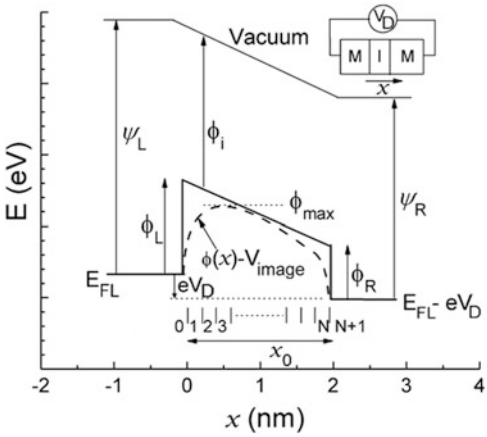

Fig. 5.2 Energy-band diagram for an asymmetric (barrier heights: $\emptyset_L \neq \emptyset_R$) tunnel barrier. The Fermi level of the left metal electrode (E_{FL}) is held fixed while that of the right electrode varies with the applied voltage (V_D). The rectangular barrier is modified by the image-force barrier lowering to give the effective barrier profile (*dashed*) [© Elsevier, [11]]

Typical diode parameters used for diodes with exponential $I(V)$ characteristics are ideality factor (η) and reverse saturation current (J_S) with $J = J_S[e^{qV/kT} - 1]$. The ideality factor is a measure of the nonlinearity, which determines how abruptly the diode turns on. The current in the device at a particular bias scales with the J_S, which is also a measure of leakage at reverse bias. Most applications require η close to one and a low J_S.

Characteristics of MIM diodes with high-barrier heights and large thicknesses are well approximated by exponential characteristics derived using the WKB approximation. However, for low-barrier diodes that are desirable for use in rectenna solar cells, the WKB approximation does not work well [11] and the characteristics are not exactly exponential. Moreover, MIM diodes may have a large current even in the reverse bias, which cannot be represented with a single exponential.

5.3.1 Resistance

Classically, resistance or more precisely differential resistance (r_D) is obtained by differentiating the dark $I(V)$ curve. A low r_D is typically needed to impedance-match the diode to the antenna. This requires the barrier heights ϕ_L and ϕ_R (each of which is the difference between the metal work function and insulator electron affinity) to be low and the insulator thickness (x_0) to be small. As discussed in Chap. 2, at high frequency, a semiclassical formula is required and gives the resistance as the reciprocal of the slope of the secant that connects two points on the dark $I(V)$ curve at $\pm V_{ph}$ around the bias voltage. Even though such a calculation usually gives a lower resistance than the classical formula, the requirement for low-barrier heights cannot be relaxed because of the large mismatch between the diode resistance and the typical antenna impedances [10].

5.3.2 Responsivity

The responsivity of a diode is a measure of how efficiently the diode can rectify. It is the curvature divided by the slope along any point on the $I(V)$ curve. For an exponential $I(V)$ curve, it is equal to the bias-independent ideality factor. Current responsivity (β) is defined as half the ratio of the second derivative of current w.r.t. voltage over the first derivative, $\beta = I''/(2I')$. The units of β are [A/W], and in the context of a rectenna, this can be viewed as the DC current generated per unit AC power incident on the diode.

To have a large responsivity requires a large curvature and/or a small slope (implying large resistance) in the $I(V)$ curve. Therefore, typically low-barrier MIM diodes tend to have smaller responsivity than high-barrier diodes. As we show in

Sect. 5.6, multi-insulator tunnel barriers give improved responsivity while keeping the resistance low.

As with resistance, the semiclassical definition of responsivity leads to a finite difference form, which in the limit of low photon energy reduces to the classical differential form, as discussed in Chap. 2. The finite difference form makes the responsivity sensitive to the asymmetry in the $I(V)$ curve around a bias voltage, as opposed to the curvature at that point.

The DC bias, which is also called the operating voltage, depends upon the application. For detectors the bias is usually positive, where the responsivity is largest, or zero, where the dark current and hence shot noise is the smallest. For energy harvesting devices such as solar cells, the bias is negative (described in Chap. 2) and is a self-bias determined by the photocurrent and load resistance.

5.3.3 Asymmetry

As explained in Chap. 3, efficient rectification requires a large forward-to-reverse current ratio. This ratio, referred to as diode asymmetry (A), is a simple measure of how well a diode can perform in a rectenna. As explained above, the semiclassical responsivity also depends on how asymmetric the $I(V)$ curve is around a particular bias point. Therefore, responsivity and asymmetry are not independent quantities, but it is useful to look at each in the appropriate context.

5.3.4 Rectification Reversal

Forward bias is defined as the bias direction for a diode junction in which a larger current flows as compared to an equivalent bias in the opposite direction. However, as explained by Eliasson [26], the direction for larger current flow may change with bias. This happens due to a transition in the dominant charge tunneling mechanism from direct to Fowler-Nordheim [27]. Direct tunneling refers to transport through the forbidden band across the whole insulator. In the Fowler-Nordheim regime, the charges tunnel through only a part of the insulator before entering the insulator conduction band. Due to a smaller tunneling distance, Fowler-Nordheim tunneling generally leads to a larger current than direct tunneling. (This Fowler-Nordheim tunneling is depicted in Figs. 2.2 and 2.3.) The transition from direct to Fowler-Nordheim regime occurs as the magnitude of bias voltage is increased in the forward or reverse direction. If the transition for reverse bias occurs at a lower voltage magnitude than for forward bias, the reverse direction may have a larger magnitude of current, implying rectification reversal.

For use in rectenna solar cells, diodes need to be designed such that rectification reversal does not occur in the operating voltage range.

5.4 MIM Diode Simulation

We assume a charge-free oxide region to determine the shape of the tunnel barrier and modify it by image-force barrier lowering. The resulting barrier shape is used to calculate the tunneling probability, which along with the Fermi distribution of electrons provides the tunnel current.

Referring to Fig. 5.2, an electron with total energy E has an x-directed component of energy E_x and a transmission probability $T(E_x)$. Assuming an isotropic distribution of electron velocities in the metal electrodes, the formula for the tunnel current from the left (cathode) to the right (anode) electrode can be written as [28]

$$J_{\mathrm{L}\to\mathrm{R}}(V_{\mathrm{D}}) = \frac{4\pi m_{\mathrm{L}} e}{h^3}\int_0^{\infty} T(E_x)\mathrm{d}E_x \int_{E_x}^{\infty} f_{\mathrm{L}}(E)\{1 - f_{\mathrm{R}}(E + eV_{\mathrm{D}})\}\mathrm{d}E \tag{5.1}$$

The Fermi-Dirac distribution functions in the left (f_{L}), and the right (f_{R}) metal electrodes are given by

$$f_{\mathrm{L}}(E) = \frac{1}{1 + \exp\left(\frac{E - E_{\mathrm{FL}}}{kT}\right)}; \quad f_{\mathrm{R}}(E + eV_{\mathrm{D}}) = \frac{1}{1 + \exp\left(\frac{E - (E_{\mathrm{FL}} - eV_{\mathrm{D}})}{kT}\right)} \tag{5.2}$$

In (5.1), the inner integral is over all possible total energies E with incident energy E_x for which there are filled states on the left and empty states on the right. The outer integral then multiplies this total number of electrons with the transmission probability $T(E_x)$ and sums the product over all E_x. The net tunnel current is the difference between the currents from the left to the right electrode ($J_{\mathrm{L}\to\mathrm{R}}$) and from the right to the left electrode ($J_{\mathrm{R}\to\mathrm{L}}$), where $J_{\mathrm{R}\to\mathrm{L}}$ can be written in a form similar to that of (5.1). Assuming effective masses in each metal region, $m_{\mathrm{L}} = m_{\mathrm{R}} = m_0$, where m_0 is the electron rest mass, the net current is given by

$$\begin{aligned} J(V_{\mathrm{D}}) &= J_{\mathrm{L}\to\mathrm{R}} - J_{\mathrm{R}\to\mathrm{L}} \\ &= \frac{4\pi m_0 e}{h^3}\int_0^{\infty} T(E_x)\mathrm{d}E_x \int_{E_x}^{\infty} \{f_{\mathrm{L}}(E) - f_{\mathrm{R}}(E + eV_{\mathrm{D}})\}\mathrm{d}E \end{aligned} \tag{5.3}$$

To calculate the transmission probability, we find a plane-wave solution for the Schrödinger equation using the transfer-matrix method (TMM) [29]. Dividing the tunnel barrier into N steps where $N \sim \mathrm{d}V/\mathrm{d}x$, the continuity condition for the wavefunction and its first derivative is applied at each interface. Unlike the basic version of a TMM [26], where a large number of 2×2 matrices need to be multiplied, the approach we use combines all the continuity equations into a $(2N + 2)$ by $(2N + 2)$ near-diagonal square matrix [30]. This method prevents round-off errors and provides numerical stability.

Applying the conditions that the amplitude of the incoming wave is unity ($A_0^+ = 1$) and that there is no reflected component in the $N + 1$th region ($A_{N+1}^+ = 1$) gives the following relation for the tunnel probability:

$$T(E_x) = \frac{k_{N+1}}{k_0} \frac{|A_{N+1}^+|^2}{|A_0^+|^2} \tag{5.4}$$

where $k_0 = \sqrt{2m_e m_L eE_x}/\hbar$ and $k_{N+1} = \sqrt{2m_e m_R eE_x}/\hbar$

For calculating $T(E_x)$, we use an adaptive step size for E_x based on the slope of $T(E_x)$. This helps preserve accuracy when required without having a very fine grid throughout. Resonance peaks are accurately tracked with this implementation.

The effective mass of the electron in the insulator (m_e) is assumed to be equal to the rest mass (m_0). This assumption is made in the absence of a more accurate estimate. For crystalline semiconductors, the m_e can be obtained from the band structure [31]. However, for the grown or deposited amorphous insulators under consideration, a direct experimental measurement is required to determine the effective mass [32].

The shape of the potential barrier is determined by the work function of the metals, the electron affinity of the insulators, and the applied voltage. This is the ideal case, but in reality surface states influence the barrier heights. In addition, an electron in the vicinity of a metal electrode experiences an image potential that causes barrier lowering, as given by (5.5) [33]:

$$V_{\text{image}}(x) = -\frac{e^2}{16\pi\varepsilon_i\varepsilon_0}\left(\frac{1}{x} + \frac{1}{x_0 - x}\right) \tag{5.5}$$

where x_0 is defined in Fig. 5.2. The magnitude of lowering is inversely proportional to the distance from the metal surfaces and the insulator dielectric constant ε_i. Equation (5.5) represents a classical concept that is correct for electrons moving near a metal plane, but its application to tunneling, which is a quantum-mechanical phenomenon, has been questioned [34]. For the quantum treatment of image potential, a number of theories have been proposed [35, 36]. Due to the lack of consensus in what has been proposed in these models, we chose to use the classical result of (5.5). From the results reported by Šunjić [36], it can be seen that the barrier lowering obtained from the quantum-mechanical image potential is smaller than that from the classical image potential. For tunnel barriers with a high dielectric constant (ε_i), V_{image} is small, which means that the difference between classical and quantum barrier lowering is minor. Hence, the choice of using the classical result for the image force is reasonable.

In the simulations we assume a perfect insulator for a solely tunneling-based analysis of the $I(V)$ characteristics. In an experimental diode, there also can be surface states, charge build up at the interfaces, and conduction through defects that can affect the current. Scattering of the electrons in the insulator also needs to be considered for thicker diodes.

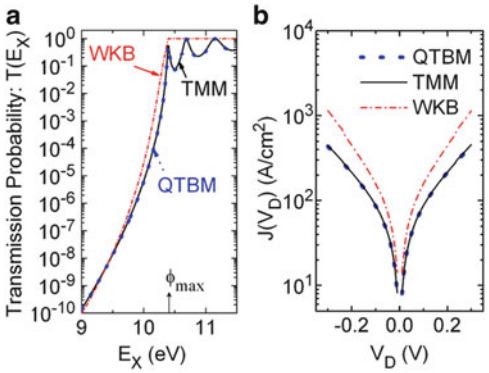

Fig. 5.3 (**a**) Log-scale plot of the transmission probability $T(E_x)$ vs. the x-directed energy of the electron (E_x) obtained from the transfer-matrix (TMM) (*solid*), the WKB (*dot-dash*), and the quantum transmitting boundary (QTBM) (*dot*) methods. (**b**) Log-scale plot of the simulated $I(V)$ characteristics of the symmetric diode. The TMM and the QTBM results match well, while the WKB predicts a higher current for the low-barrier diode

5.4.1 Comparison with Other Simulation Techniques

We compare the transmission probability calculated by the TMM, with those obtained from the WKB approximation, which is dated but has been used recently [37], and the more current quantum transmitting boundary method (QTBM) [38]. Consider a symmetric tunnel barrier with insulator thickness $x_0 = 2$ nm, $\Phi_L = \Phi_R = 0.5$ eV and $E_{FL} = 10$ eV, where E_{FL} is the Fermi level referenced to the bottom of the conduction band in the left metal. The electron wavefunction for $E_x < \Phi_{max}$, where Φ_{max} is the highest potential on the modified barrier as shown in Fig. 5.2, decays with increasing x inside the barrier. The $T(E_x)$ rises sharply with increasing energy, as seen in the plot of Fig. 5.3a.

When the electron energy (E_x) rises above the barrier (Φ_{max}), the wavefunction becomes oscillatory and the transmission probability stays close to unity. For $E_x > \Phi_{max}$, there are resonances in $T(E_x)$ due to interference of the wavefunction inside the insulator.

The TMM calculation of $T(E_x)$ is in close agreement with the WKB approximation for $E_x < E_{FL}$ (10 eV). However, at higher energy, the WKB overestimates the transmission probability and gives $T(E_x) = 1$ for $E_x > \Phi_{max}$. As shown in Fig. 5.3b, this results in a significant deviation of $I(V)$ characteristics on using the WKB method. On the other hand, in both the figures, there is no difference between the results obtained from the TMM and the QTBM, both of which give solutions to the Schrödinger equation. Therefore, analytical formulae for tunnel current obtained using the WKB approximation are not applicable to low-barrier MIM diodes [28].

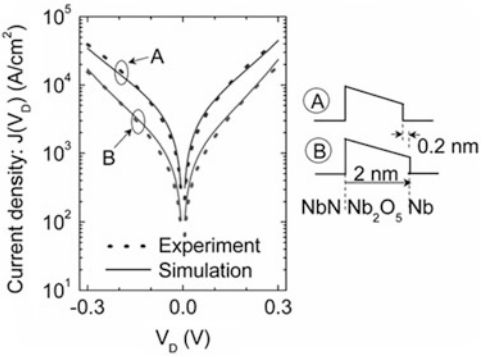

Fig. 5.4 Comparison of simulated and experimental $I(V)$ characteristics for two MIM diodes. The simulated curves obtained from the transfer-matrix method are in close agreement with experimental characteristics. The insulator widths used in the diode simulations are as targeted during deposition [© Elsevier, [11]]

5.4.2 Comparison with Experimental Characteristics

Simulated and experimental characteristics of two asymmetric-MIM diodes are compared in Fig. 5.4. The diodes are made from sputtered insulator and metal layers, and the dimensions shown are the targeted thickness of the insulators. The simulated $I(V)$ curves are in good agreement with the measured characteristics. The simulated and the experimental curves match well without the use of any fitting parameters besides the choice of effective mass equal to the rest mass. The parameters for the materials, used in the simulation and given in the table below, are either book values or extracted from measurements [39].

Metal	Work function (eV)	Insulator	Electron affinity (eV)	Dielectric constant
Nb	4.33	Nb_2O_5	4.23	25
NbN	4.7	Ta_2O_5	3.83	20

5.5 Single-Insulator (MIM) Diodes

Using the simulation methodology described above, we now analyze the properties of a single-insulator diode in more detail. A closer look at how the barrier height affects the tunnel current is facilitated by comparing two diodes with different barrier heights. We develop an understanding for the temperature dependence of tunnel current that arises due to the Fermi distribution. Finally, we look at the temperature variation of current for different barrier heights.

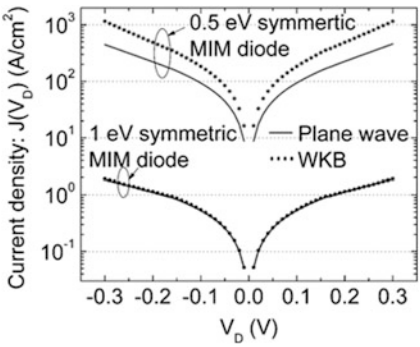

Fig. 5.5 Simulated $I(V)$ curves for two symmetric MIM diodes simulated using different methods. The insulator thickness is 2 nm for both diodes while the barrier heights are 0.5 and 1 eV

5.5.1 *Barrier Height Dependence of Tunnel Current*

As given by (5.3), the Fermi distribution and the transmission probability of electrons tunneling across the barrier together determine the tunnel current. For two diodes that differ only in their barrier heights, the Fermi distribution is identical, but the transmission probability is different. To explain the dependence of tunnel current on the barrier height, consider a low-barrier (0.5 eV) and a high-barrier (1 eV) diode. Referring to Fig. 5.2, $\Phi_{\max}$ is closer to the Fermi level on the left side (E_{FL}) in the low-barrier case. Therefore, as seen in Fig. 5.3a, the sharp peak in $T(E_x)$ near $E_x = \Phi_{\max}$ adds significantly to the tunnel current only in the low-barrier diode. In the high-barrier diode, this rise in $T(E_x)$ is insignificant, as the Fermi distribution causes the concentration of tunneling electrons to be several orders of magnitude smaller than for the low-barrier. This leads to a smaller tunnel current in the high-barrier diode.

To show that the contribution of electrons near $\Phi_{\max}$ is dominant only in the low-barrier case, we compare the tunnel currents calculated using the $T(E_x)$ obtained from the plane-wave solution and the WKB approximation in Fig. 5.5.

This comparison provides physical insights regarding the sensitivity of the tunnel current to an inaccurate estimate of $T(E_x)$ near the peak of the barrier. The sensitivity decreases with increasing barrier height as the contribution of electrons near the peak of the barrier reduces. As shown in Fig. 5.3a, the WKB overestimates the transmission probability around $\Phi_{\max}$, and hence it should give a higher estimate for the tunnel current than the TMM. In the low-barrier (0.5 eV) diode, WKB predicts higher current than the plane-wave method. However, for the high-barrier diode (1 eV), the WKB and plane-wave results are in agreement. The above results show that in the high-barrier case, the electrons near $\Phi_{\max}$ have a smaller contribution to the total current. Again, this shows the limited validity of the WKB method, which is accurate only for high-barrier diodes. It also makes clear the inapplicability of analytical formulae for analyzing tunnel current in low-barrier diodes.

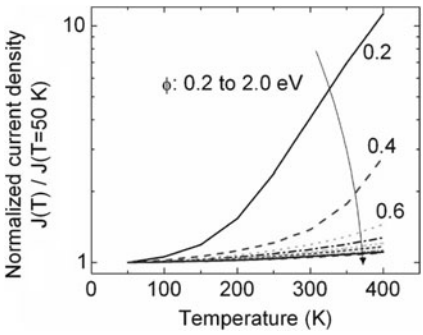

Fig. 5.6 Normalized current density vs. temperature for a range of barrier heights in a symmetric MIM diode biased at 0.3 V. The temperature dependence is larger for smaller barriers. The change in current with barrier height increases as the temperature rises

5.5.2 *Temperature Dependence of Tunnel Current*

In addition to determining the energy range of electrons that contribute to the tunnel current, the Fermi distribution also determines the temperature dependence of the tunnel current. As the temperature rises, the spread in the Fermi distribution causes a larger contribution from the high-(above E_{FL}) energy electrons. Electrons at higher energies have a greater probability of tunneling across the barrier. Therefore, at higher temperature, the increased concentration of high-energy electrons and their greater probability of tunneling result in a larger tunnel current. At low-barrier heights and high temperatures, there may be significant thermionic emission above the barrier. This component of current has been ignored as we are investigating the temperature dependence of only the tunnel current.

The dependence on temperature is stronger at lower-barrier heights. To demonstrate this trend, we calculate the tunnel current at various temperatures and for a range of barrier heights in Fig. 5.6.

We consider symmetric tunnel junctions ($\Phi_L = \Phi_R = \Phi$) of barrier heights varying from 0.2 to 2 eV. The insulators are 2 nm thick, and the temperature is varied from 50 to 400 K. To compare all barriers on a common scale, the current density is normalized by its value at 50 K for each barrier height and is plotted in Fig. 5.6. The variation with temperature is larger for smaller barriers. This happens because the tail of the Fermi distribution is significant near the top of the barrier, where the transmission probability is also high.

The temperature dependence of current can be reduced to a power-law relation of the type

$$y = ax^b + c \tag{5.6}$$

The data of Fig. 5.6 is fitted to (5.6) and compared with the analytically obtained [2] temperature dependence of the form

$$\frac{J(T \neq 0)}{J(T = 0)} = \frac{\pi c_1 kT}{\sin(\pi c_1 kT)} = 1 + \frac{1}{6}(\pi c_1 kT)^2 + \cdots \tag{5.7}$$

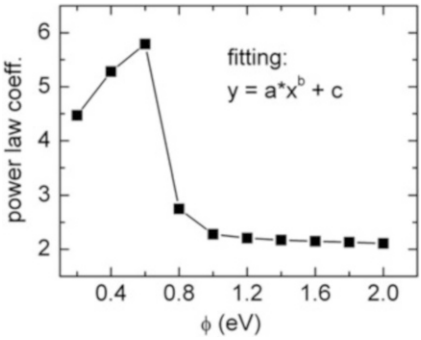

Fig. 5.7 Power-law coefficient b vs. barrier height from the curve fit for temperature dependence of tunnel current. For the 2 nm diode under consideration, only for barrier heights greater than 0.8 eV does the temperature dependence become quadratic as predicted by the analytical formula (5.7)

where c_1 is a function of the barrier shape. In (5.7) the coefficient b is 2. The actual power-law temperature dependence of current at low-barrier heights is greater than 2 as seen in Fig. 5.7.

The coefficient c in (5.6) is 1 within a 5 % margin, indicating the accuracy of the curve fitting. Diodes with low barriers have highly temperature-dependent tunnel currents. Only for barrier heights greater than 0.8 eV does the behavior start to exhibit the quadratic temperature dependence given in (5.7). This observation is dependent on several variables including the temperature range in consideration and the width of the barrier. Nonetheless, it signifies that the analytical formula does not provide the correct temperature dependence for low-barrier diodes.

5.5.3 *Shortcomings of MIM Diodes*

Eliasson [26] extensively analyzed the possible variations of a single-insulator MIM diode. The $I(V)$ characteristics of the diode depend on the shape of the tunnel barrier, which is determined by the metals and insulators used to form the diode. To optimize the MIM diode, the variable parameters are the barrier heights Φ_L, $\Phi_{R,}$ and the insulator thickness. The characteristics that typically need to be optimized are the differential resistance and responsivity of the diode.

As stated before, a low resistance is necessary to ensure efficient coupling of the diode to the antenna and is achieved by keeping the barrier heights low [26]. A high responsivity is required for efficient square-law (small signal) rectification [9]. Here we analyze these characteristics at zero bias, which reduces the complexity of comparing the resistance and responsivity of several diodes. At zero bias, the responsivity is determined by the degree of asymmetry in the shape of the tunnel barrier, which causes the asymmetry in the $I(V)$ curve. In Fig. 5.8a, b, we plot the responsivity and resistance vs. the difference in barrier height on the left (Φ_L)and the right (Φ_R). Experimentally, this can be achieved by varying the metal on the left while keeping the insulator and the metal on the right fixed.

As explained in Chap. 2, an asymmetric $I(V)$ is necessary for self-bias generation and efficient rectification. The zero-bias responsivity is an indicator of this

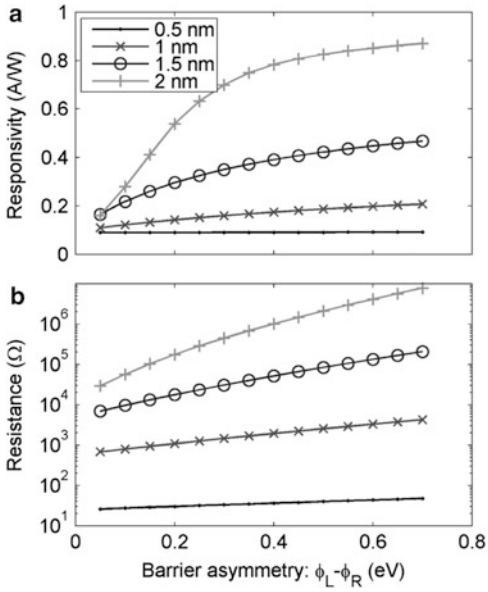

Fig. 5.8 (**a**) Responsivity and (**b**) resistance at zero bias vs. barrier asymmetry for MIM diodes. The diode thickness and the left barrier height (Φ_L) are varied while the right barrier height (Φ_R) is kept fixed at 0.1 eV. The responsivity increases with increasing asymmetry but saturates for high $\Phi_L - \Phi_R$. For the same asymmetry, the responsivity is larger for thicker diodes. Increasing asymmetry and increasing thickness lead to larger resistance [© Elsevier, [11]]

asymmetry. As seen in Fig. 5.8a, for a fixed asymmetry, the responsivity is higher for thicker barriers. Also, the thicker barriers show a greater change in responsivity with increasing asymmetry. However, the responsivity saturates at large asymmetry. As the responsivity increases with increasing asymmetry or increasing thickness, so does the resistance as shown in Fig. 5.8b. In a rectenna, this negates the improvement in responsivity as the impedance match between the antenna and the diode becomes worse.

A nonzero responsivity at zero bias is an indicator of the asymmetry in the diode $I(V)$ curve, which is necessary for rectenna solar cells, as explained in Chap. 2. However, the above characteristics are not representative of responsivity at a nonzero bias, which may be sufficient for the operation of a biased detector. Little or no responsivity at zero bias does not preclude the possibility that the asymmetry in the $I(V)$ occurs at nonzero bias voltages.

Characteristics of MIM diodes can be improved through the design of multi-insulator tunnel diodes, as discussed next.

5.6 Double-Insulator (MIIM) Tunnel Diodes

Depending on the application, a diode with a high forward-to-reverse current ratio (asymmetry) or a sharp turn-on (nonlinearity) may be required. As analyzed in Chap. 2, low-resistance MIM tunnel diodes fail to achieve these requirements. Well-engineered multi-insulator diodes can have improved $I(V)$ characteristics satisfying both these requirements. We analyze two mechanisms that can improve the performance of multi-insulator diodes. Either of these mechanisms can be made

to dominate by the appropriate choice of insulators and barrier thicknesses. Two double-insulator (MIIM) diodes based on these mechanisms are simulated, and their characteristics are compared with MIM diodes.

Hegyi et al. [40] conducted a simulation-based investigation of parameters for an optimized MIIM diode. However, their implementation did not include the effect of resonant tunneling [26], which may significantly alter the diode behavior. In another MIIM configuration [41], an abrupt change in tunnel distance with increasing bias voltage leads to a high forward-to-reverse current ratio. We develop an in-depth understanding of these effects and use them to design MIIM diodes with improved characteristics for high-frequency rectennas.

5.6.1 Simulation Methodology

In Sect. 5.4, we gave the framework for simulating MIM diodes using the TMM. The same methodology is applicable to a multi-insulator barrier profile. However, in a multi-insulator diode, the dielectric constants of the insulators play an important role in determining the voltage drop across each insulator layer. To determine the energy-band profile at a certain bias (V_D), we apply the condition for continuity of the electric displacement vector at each insulator interface and obtain the voltage drop across each layer:

$$\Delta V_j = (V_D - V_{bi}) \frac{x_j/\varepsilon_j}{\sum x_j/\varepsilon_j} \tag{5.8}$$

where x_j and ε_j represent the thickness and dielectric constant, respectively, of the jth layer and eV_{bi} ($=\psi_L - \psi_R$) is the built-in potential.

In a multi-insulator diode, extending (5.5), the effect of the classical image force is calculated as

$$V_{image}(x) = -\frac{e^2}{16\pi\varepsilon_0}\left(\frac{1}{\int_0^x \varepsilon(x')\mathrm{d}x'} + \frac{1}{\int_x^L \varepsilon(x')\mathrm{d}x'}\right) \tag{5.9}$$

where the integration limit L is the total thickness of the barrier. The integrals in the denominator represent the effective distance of an electron from the left or the right metal electrode while accounting for the changing dielectric constant.

An effect of interest in multi-insulator diodes is that of resonant tunneling of electrons through a quantum well, which is accounted for in the TMM described in Sect. 5.4.

5.6.2 Double-Insulator Configurations

To obtain a high-responsivity and low-resistance diode, one can design an MIIM barrier with resonant tunneling [26, 42]. Alternatively, an MIIM configuration can

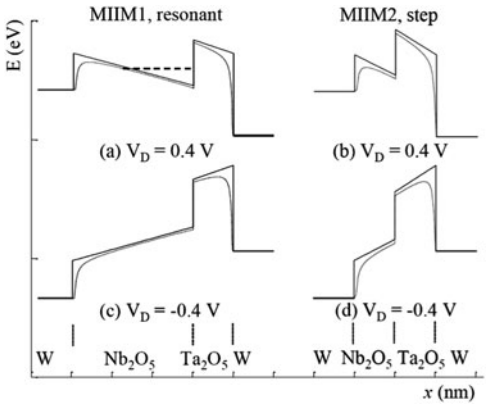

Fig. 5.9 Energy-band profiles for the resonant and step MIIM diodes. Forward and reverse bias profiles are shown, respectively, in (**a**) and (**c**) for the resonant and in (**b**) and (**d**) for the step diode. The *dotted lines* show the profiles with barrier lowering. The thickness of the Nb_2O_5 layer is the only structural difference between the two diodes [© Elsevier, [11]]

be designed to have a step change in tunnel distance (with increasing voltage) for electrons tunneling from the higher Fermi level [41]. Both these mechanisms can occur in the same diode, and the overall asymmetry of the $I(V)$ curve is regulated by the one that dominates. We examine these effects through the simulation of two double-insulator tunnel diodes.

Consider two MIIM diodes that have the same material configuration but different insulator thicknesses. For the two diodes, the conduction band profiles under positive and negative bias are shown in Fig. 5.9.

Diode MIIM1 consists of W-Nb_2O_5(3 nm)-Ta_2O_5(1 nm)-W, and MIIM2 consists of W-Nb_2O_5(1 nm)-Ta_2O_5(1 nm)-W. The material parameters for the oxides were listed in Sect. 5.4.2. The work function of tungsten is 4.55 eV [43]. This choice of materials and dimensions is not optimized for maximum nonlinearity or current but rather is chosen to demonstrate the difference between the resonant tunneling dominant in MIIM1 and the step change dominant in MIIM2.

A quantum well is formed in both MIIM diodes under positive bias (a) and (b). However, only in the MIIM1, the quantum well is wide enough to produce a resonant energy level. On the other hand, under negative bias (c) and (d), the step barrier profile leads to an abrupt decrease in the tunneling distance for the electrons near the Fermi level on the right metal electrode with increasing reverse bias. The Fermi level on the left metal electrode is fixed at 10 eV.

In Fig. 5.10, we plot the transmission probability $T(E_x)$ and the current density $J(E_x)$ for the four barrier profiles of Fig. 5.9.

We first discuss $T(E_x)$ comparing the curves on the basis of the barrier shapes and the applied voltages. Due to the magnitude of the bias voltages, the negative-bias curves in Fig. 5.10 are offset along the energy axis from those at positive bias by approximately 0.4 eV. The fact that the offset is 0.4 eV instead of the difference between the biases (0.8 eV) is explained by the reciprocity of $T(E_x)$. In Fig. 5.9, if the barrier profiles at negative voltages are flipped along the x-direction, the difference in Fermi levels between the barrier profiles of opposite bias is 0.4 eV and hence the offset. For low-electron energies, the transmission

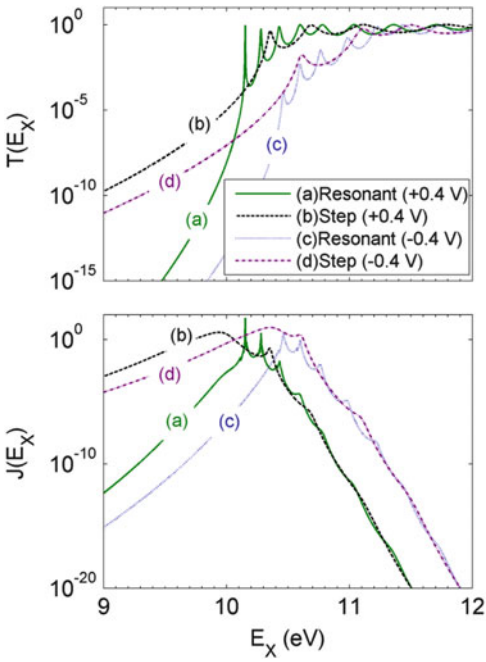

Fig. 5.10 Electron transmission probability $T(E_x)$ and current density $J(E_x)$ vs. energy for the resonant and step MIIM diodes of Fig. 5.9. A sharp resonance peak is observed in the resonant diode at forward bias due to the formation of a quantum well [© Elsevier, [11]]

probability $T(E_x)$ for the step (MIIM2) diode, represented by curves (b) and (d), is higher than for the resonant (MIIM1) diode, represented by (a) and (c). This is because it is easier to tunnel across a thin barrier than a thick one.

The resonant diode under positive bias (a) has a sharp rise in $T(E_x)$ exceeding (b) at the resonance peak. Except for the resonance peak, the $T(E_x)$ near the top of the barriers, $E_x > 10$ eV for (a) and (b) and $E_x > 10.4$ eV for (c) and (d), is almost equal for the two diodes. As E_x rises above the highest potential on the low-barrier insulator, the transmission probability exhibits oscillatory behavior for all four cases. In this energy range, the electron wavefunction exponentially decays while tunneling and is sinusoidal through the remaining region of transmission above the conduction band. The sinusoidal wavefunction resonates with the edges of the tunnel barrier causing the oscillations in $T(E_x)$. These oscillations modify the probability of tunneling through the higher barrier to give the net $T(E_x)$.

The above trends in $T(E_x)$ influence the current density $J(E_x)$. The area under the resonant diode $J(E_x)$ at positive bias (a) is greater than at negative bias (c). Therefore, the current in the resonant diode is greater at positive bias, as shown in the $I(V)$ curve of Fig. 5.11a. For the step diode, the area under the $J(E_x)$ curve at negative bias (d) is greater than under positive bias (b). This asymmetry is also seen in the $I(V)$ curve shown in Fig. 5.11a. Comparing the resonant and the step diode $J(E_x)$ curves, the narrow resonance peak in (a) is large enough to give a current greater than that in the step diode under positive bias (b) but not enough to exceed the current in the step diode under negative bias (d).

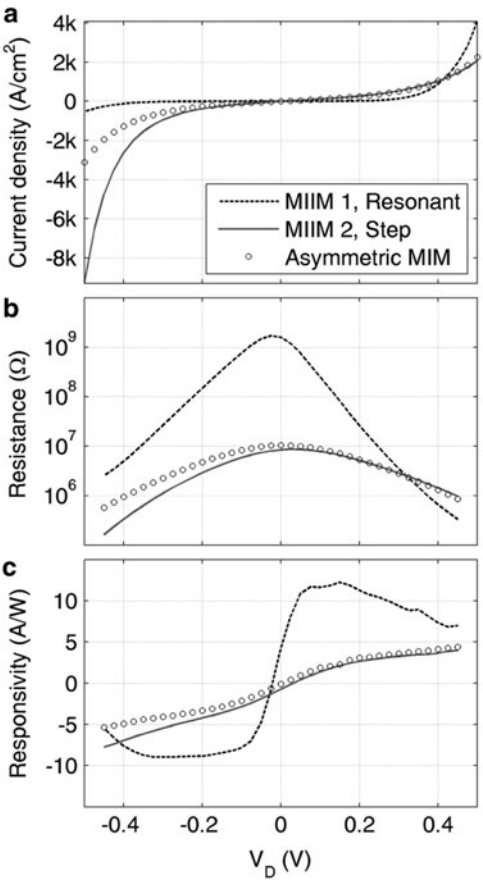

Fig. 5.11 (**a**) Current density vs. voltage for the MIIM diodes shown in Fig. 5.9 and a comparable asymmetric-MIM diode. The step MIIM diode has higher current magnitude under negative bias due to the direct tunneling of electrons across the high barrier. The resonant MIIM diode has the opposite asymmetry in its $I(V)$ characteristic, due to the formation of resonant quantum well under positive bias. Comparing these with the asymmetric-MIM diode, we see that both the MIIM diodes have a smaller resistance (**b**) and larger nonlinearity (**c**) in their preferred direction of conduction [© Elsevier, [11]]

In Fig. 5.11a, we also compare the MIIM diodes with an asymmetric-MIM diode that has barrier heights corresponding to the W-Nb_2O_5 interface on the left and the Ta_2O_5-W interface on the right and an insulator thickness of 2 nm. The asymmetric-MIM diode is essentially the MIIM2 diode without the abrupt step in the conduction band profile. This is confirmed by their similar current densities under positive bias. However, under negative bias, the step change in tunnel distance in MIIM2 causes a sharp increase in tunnel current. This difference is also evident in the resistance and responsivity curves in Fig. 5.11b, c where, under negative bias, the sharp increase in current for MIIM2 leads to a lower resistance and a higher responsivity. The resistance of the resonant diode is significantly higher at zero bias but becomes comparable to the thinner diodes near $V_D = 0.4$ V. The large change in resistance also accounts for the higher magnitude of responsivity. Thus, the nonlinearity improving mechanisms enable MIIM diodes with higher responsivity and lower differential resistance than an equivalent MIM diode of comparable current density.

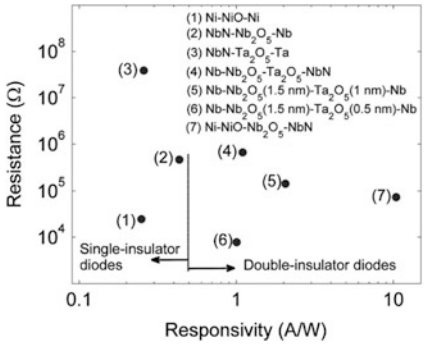

Fig. 5.12 Resistance vs. responsivity at zero bias for single- and double-insulator diodes. Antenna-coupled diode detectors require high responsivity and low resistance. The double-insulator diodes show improved performance, having smaller resistance and larger responsivity. The area for the diodes is 100×100 nm^2

5.6.3 Comparison of MIM and MIIM Diodes

The above example shows that just changing the thickness of an insulator in an MIIM diode made with the same pair of materials can lead to different asymmetry and nonlinearity. It does not suggest which of the mechanisms for achieving larger nonlinearity is preferable. We have analyzed several MIIM diodes designed for implementing these mechanisms, and the performance improvement over MIM diodes is observed consistently. The mechanisms exemplified in MIIM diodes can also be applied to barriers with more than two insulators [44, 45].

The comparison of thick and thin double-insulator diodes shows that the bias direction causing higher current depends on the electron transmission-limiting mechanism. Defining positive bias as that which produces or augments a quantum well at the interface between the insulators, if a resonant energy level is achievable, the current for this polarity can become larger than that under negative bias. In the absence of a resonant level, the step change in tunneling distance under negative bias causes a larger current than under positive bias. Compared to single-insulator diodes, the resonance and the step mechanisms in double-insulator diodes result in a larger responsivity and a smaller resistance.

In Fig. 5.12, we compare the resistance vs. responsivity at zero bias for several single- and double-insulator diodes. The simulations show that for comparable resistance values, the responsivity of double-insulator diodes is larger than that of single-insulator diodes. Therefore double-insulator devices are able to achieve both the desirable characteristics, whereas single-insulator diodes are limited in their responsivity.

References

1. Kroemer H. Quantum mechanics. Englewood Cliffs, NJ: Prentice-Hall; 1994.
2. Stratton R. Volt-current characteristics for tunneling through insulating films. J Phys Chem Solids. 1962;23(9):1177–90.
3. Nagae M. Response time of metal-insulator-metal tunnel junctions. Jpn J Appl Phys. 1972;11 (11):1611–21.
4. Simmons JG. Conduction in thin dielectric films. J Phys D Appl Phys. 1971;4(5):613.
5. Riccius HD. Improved metal-insulator-metal point-contact diodes for harmonic generation and mixing. Appl Phys A. 1978;17(1):49–52.
6. Periasamy P, Bergeson JD, Parilla PA, Ginley DS, O'Hayre RP. Metal-insulator-metal point-contact diodes as a rectifier for rectenna. In 35th IEEE Photovoltaic Specialists Conference (PVSC), Honolulu, HI; 2010. p. 2943–5.
7. Riccius HD, Siemsen KJ. Point-contact diodes. Appl Phys Mater Sci Process. 1984;35:67–74. doi:10.1007/BF00620632.
8. Evenson KM, Wells JS, Matarrese LM, Elwell LB. Absolute frequency measurements of the 28- and 78- μm cw water vapor LASER lines. Appl Phys Lett. 1970;16(4):159–62.
9. Sanchez Jr A, Davis CF, Liu KC, Javan A. The MOM tunneling diode: theoretical estimate of its performance at microwave and infrared frequencies. J Appl Phys. 1978;49(10):5270–7.
10. Grover S, Moddel G. Applicability of metal/insulator/metal (MIM) diodes to solar rectennas. IEEE J Photovoltaics. 2011;1(1):78–83.
11. Grover S, Moddel G. Engineering the current-voltage characteristics of metal-insulator-metal diodes using double-insulator tunnel barriers. Solid State Electron. 2012;67(1):94–9.
12. Daneu V, Sokoloff D, Sanchez A, Javan A. Extension of laser harmonic-frequency mixing techniques into the 9 micron region with an infrared metal-metal point-contact diode. Appl Phys Lett. 1969;15(12):398–401.
13. Grover S, Dmitriyeva O, Estes MJ, Moddel G. Traveling-wave metal/insulator/metal diodes for improved infrared bandwidth and efficiency of antenna-coupled rectifiers. IEEE Trans Nanotechnol. 2010;9(6):716–22.
14. Estes MJ, Moddel G. Terahertz interconnect system and applications. US Patent 6,967,347; 2005.
15. Fumeaux C, Herrmann W, Kneubühl FK, Rothuizen H. Nanometer thin-film Ni-NiO-Ni diodes for detection and mixing of 30 THz radiation. Infrared Phys Technol. 1998;39 (3):123–83.
16. Abdel Rahman MR, Gonzalez FJ, Zummo G, Middleton CF, Boreman GD. Antenna-coupled MOM diodes for dual-band detection in MMW and LWIR. Proc SPIE. 2004;5410:238–43.
17. Rockwell S, et al. Characterization and modeling of metal/double-insulator/metal diodes for millimeter wave wireless receiver applications. In Radio frequency integrated circuits (RFIC) symposium, IEEE, Honolulu, HI; 2007. p. 171–174.
18. Wang SY, Izawa T, Gustafson TK. Coupling characteristics of thin-film metal-oxide-metal diodes at 10.6 μm. Appl Phys Lett. 1975;27(9):481–3.
19. Codreanu I, Gonzalez FJ, Boreman GD. Detection mechanisms in microstrip dipole antenna-coupled infrared detectors. Infrared Phys Technol. 2003;44(3):155–63.
20. Yamagishi H, et al. Antenna-coupled rectifying diode for IR detection. Proc SPIE. 2005;2882:102–10.
21. Kazemi H, et al. First THz and IR characterization of nanometer-scaled antenna-coupled InGaAs/InP Schottky-diode detectors for room temperature infrared imaging. Proc SPIE. 2007;6542(1):65421.
22. Marchetti S, Sandri P, Simili R. Theoretical and experimental responsivity of FIR antenna coupled metal-insulator-metal detectors. Int J Infrared Millimeter Waves. 1997;18 (7):1395–409.

23. Tiwari B, et al. Controlled etching and regrowth of tunnel oxide for antenna-coupled metal-oxide-metal diodes. J Vacuum Sci Technol B Microelectron Nanometer Struct. 2009;27(5):2153–60.
24. Estes MJ, Eliasson BJ, Moddel G, private communication, Phiar Corporation 2007.
25. Hobbs PC, Laibowitz RB, Libsch FR, LaBianca NC, Chiniwalla NC. Efficient waveguide-integrated tunnel junction detectors at 1.6 μm. Opt Express. 2007;15 (25):16376–89.
26. Eliasson BJ. Metal-insulator-metal diodes for solar energy conversion. PhD Thesis, University of Colorado at Boulder, Boulder; 2001.
27. Fowler RH, Nordheim L. Electron Emission in Intense Electric Fields. Proc R Soc Lond Ser A. 1928;119(781):173–81.
28. Simmons JG. Generalized formula for the electric tunnel effect between similar electrodes separated by a thin insulating film. J Appl Phys. 1963;34(6):1793–803.
29. Jonsson B, Eng ST. Solving the Schrodinger equation in arbitrary quantum-well potential profiles using the transfer matrix method. IEEE J Quantum Electron. 1990;26(11):2025–35.
30. Probst OM. Tunneling through arbitrary potential barriers and the apparent barrier height. Am J Phys. 2002;70(11):1110–6.
31. Kittel C. Introduction to solid state physics. 7th ed. New York: Wiley; 1996.
32. Solymar L, Walsh D. Electrical properties of materials. 8th ed. New York: Oxford University Press; 2010.
33. Sze SM, Ng KK. Physics of semiconductor devices. 3rd ed. San Jose, CA: Wiley-Interscience; 2006.
34. Hartstein A, Weinberg ZA. On the nature of the image force in quantum mechanics with application to photon assisted tunnelling and photoemission. J Phys C Solid State Phys. 1978;11(11):L469.
35. Puri A, Schaich WL. Comparison of image-potential theories. Phys Rev B. 1983;28 (4):1781–4.
36. Šunjić M, Marušić L. Dynamical effects in electron tunneling: self-consistent semiclassical image potentials. Phys Rev B. 1991;44(16):9092–5.
37. Chapline MG, Wang SX. Analytical formula for the tunneling current versus voltage for multilayer barrier structures. J Appl Phys. 2007;101(8):083706.
38. Lent CS, Kirkner DJ. The quantum transmitting boundary method. J Appl Phys. 1990;67 (10):6353–9.
39. Corporation Phiar. Private communication; 2007.
40. Hegyi B, Csurgay A, Porod W. Investigation of the nonlinearity properties of the DC I-V characteristics of metal-insulator-metal (MIM) tunnel diodes with double-layer insulators. J Comput Electron. 2007;6:159–62. doi:10.1007/s10825-006-0083-9.
41. Matsumoto Y, Hanajiri T, Toyabe T, Sugano T. Single electron device with asymmetric tunnel barriers. Jpn J Appl Phys. 1996;35:1126–31.
42. Moddel G, Eliasson B. High speed electron tunneling device and applications. U.S. Patent No. 6,756,649; 2004.
43. Camp M, Lecchini SMA. The work function of polycrystalline tungsten foil. Proc Phys Soc. 1965;85(4):815.
44. Korotkov A, Likharev K. Resonant Fowler-Nordheim tunneling through layered tunnel barriers and its possible applications. In Technical Digest IEDM, Washington, DC; 1999. p. 223–226.
45. Maraghechi P, Foroughi-Abari A, Cadien K, Elezzabi AY. Enhanced rectifying response from metal-insulator-insulator-metal junctions. Appl Phys Lett. 2011;99:253503.